Smart Mater. Struct. **9** (2000) 701–710. Printed in the UK PII: S0964-1726(00)14319-8

In situ displacement measurements and numerical predictions of embedded SMA transformation

K D Jonnalagadda†§, N R Sottos†, M A Qidwai‡‖ and D C Lagoudas‡

† Department of Theoretical and Applied Mechanics, University of Illinois Urbana-Champaign, Urbana, IL 61801, USA
‡ Center for Mechanics of Composites, Aerospace Engineering Department, Texas A&M University, College Station, TX 77843, USA

Received 13 December 1999, in final form 16 May 2000

Abstract. The transformation behavior of an embedded shape memory alloy (SMA) ribbon was investigated experimentally and numerically. Single SMA ribbons (55% Ni, 45% Ti) were pre-strained to 1% and then embedded in a room-temperature-cured epoxy resin. The embedded ribbons were heated resistively to a temperature above the austenite start temperature to induce transformation. The development of displacements and strains due to transformation were measured *in situ* using moiré interferometry. Analysis of the resulting fringe patterns at steady-state temperature and after cool down indicated that most of the phase transformation in the embedded SMA ribbon was restricted to a region close to the edge of the sample. Numerical simulation of the embedded ribbon was carried out using a fully-coupled thermomechanical SMA constitutive model. Numerical predictions were in good agreement with both the measured displacements and strains in the ribbon and confirmed that only the outer edges of the ribbon transform due to the constraint imposed by the polymer matrix.

1. Introduction

The shape memory effect was first discovered over 50 years ago in a gold–cadmium alloy [1]. The effect was later observed in nickel–titanium alloys of nearly equiatomic composition by Buehler *et al* of the Naval Ordinance Laboratories in 1963 [2]. Since then, other shape memory alloys (SMAs) such as Cu–Zn–Al have also been discovered. Alloys which exhibit the shape memory effect are capable of recovering large strains (up to 10%) as a result of martensitic transformation. The amount of recovery depends on the temperature, the initial deformation and the percentage of the martensite phase that is present in the material. Restraining a SMA from regaining its original shape produces significant recovery stresses. The large strain recovery properties have led to many unique applications of SMAs, including uses as actuators for active stiffness, shape and vibration control of smart structures.

Numerous metallurgical and crystallographic studies have resulted in a thorough understanding of the micromechanical aspects of the shape memory effect. Shape memory materials undergo a diffusionless, isochoric, solid–solid transformation between an austenite and martensite phase [3]. When heated, a SMA transforms to the austenite phase, which has a body-center cubic (bcc) microstructure. Upon cooling, the SMA transforms to a martensite phase with a less rigid monoclinic structure, which permits the coexistence of multiple variants of martensite. The transformation involves two processes—the Bain strain and the lattice-invariant shear. The Bain strain incorporates the small movements of atoms needed to produce the new crystal structure of martensite. The lattice-invariant shear mechanism accommodates the different shape of the new martensite within the transformed austenite. The uniqueness of shape memory lies in the fact that the lattice-invariant shear step of this transformation occurs almost solely by twinning [3]. Twinning forces the bcc structure into a tilted monoclinic structure with alternate bands, creating a herringbone effect. When stress is applied to this structure, the alternate bands align in the same direction by a process called detwinning. When the material is again heated to the austenitic phase, the detwinned crystal structure transforms back to the bcc austenite and regains its original shape. Because no slip or dislocation entanglements have been introduced into the microstructure during the cooling or deformation stage, the process is reversible.

Applied stress and temperature have a significant effect on the transformation characteristics of SMAs [3, 4]. A decrease in temperature has the same effect as an increase in stress, both stabilizing martensite. The temperatures

§ Current address: Motorola Labs, Motorola Advanced Technology Center, Room 1014, 1301 Algonquin Road, Schaumburg, IL 60196, USA.
‖ Current address: Multifunctional Materials Group, Code 6350, Naval Research Lab, 4555 Overlook Ave SW, Washington, DC 20375, USA.

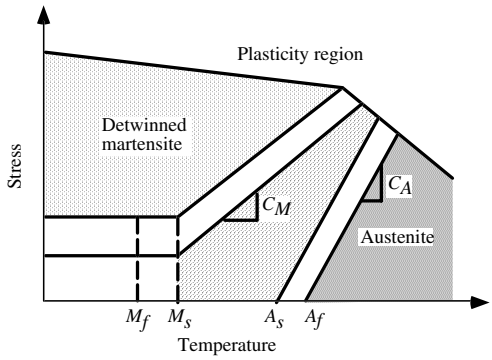

Figure 1. Schematic phase diagram of SMA showing the effect of applied stress on the transformation temperatures.

characterizing the start and finish of transformation are the austenite start (A_s), austenite finish (A_f), martensite start (M_s) and martensite finish (M_f). The transformation temperatures increase linearly with applied stress as shown schematically by the phase diagram in figure 1 [3, 5, 6]. The slopes C_M and C_A are the stress–temperature coefficients for martensite and austenite, respectively. Linear behavior is observed until the movement of dislocations in the crystal structure becomes energetically more favorable than the formation of the stress-induced martensite.

Since the discovery of the shape memory effect, a significant amount of research has been devoted to characterizing and modeling macroscopic (continuum-level) SMA behavior. Comprehensive uniaxial mechanical test data of polycrystalline SMA wires and bars subject to various stress and temperature cycles have been reported by Shaw and Kyriakides [7, 8], Leo *et al* [9], Dalaey and Thienel [10], Miyazaki *et al* [11, 12], Ling and Kaplow [13], Jackson *et al* [14], Wasilewski [15], Buehler *et al* [2] and many others. Considerable effort has also been directed toward development of phenomenological models to describe the thermo-mechanical evolution of a SMA. Bekker and Brinson [6] provide an excellent review of the various models and propose four groups for classification: (i) 1D and 2D models based on the Landau/Landau–Ginzburg free energy formulation, (ii) 1D models developed to study dynamics of phase boundary motion, (iii) 1D constitutive models which employ a quasi-static kinetic law and (iv) self-consistent meso/macroscale models based on phase-mixture theory formulated in terms of free energy.

SMAs in the form of wires, ribbons or thin films can also be embedded in a host material to form a SMA composite. Initial attempts by Liang *et al* [16] to embed nitinol wires into polymers proved largely unsuccessful due to poor interfacial bonding. Subsequently, Baz and Ro [17] and Chaudry and Rogers [18] incorporated SMA wires using coupling sleeves and mechanical fasteners, respectively. Hebda *et al* [19] successfully embedded two-way trained wires in a composite and examined issues in manufacturing, such as void content and SMA training effects.

Only a few investigations in the literature have focused on the behavior of SMAs embedded in a host material. The interaction between the embedded SMA and the surrounding material is critical since most applications require transfer of load or strain from the wire to the host. Paine *et al* [20] and Paine and Rogers [21] asserted the importance of interfacial adhesion between embedded SMA wires and the host material. Bidaux *et al* [22] measured significant differences in dynamic behavior between free-standing SMA wires and SMA wires embedded in a polymer composite. The change in response was analyzed in terms of the SMA–matrix interaction. Paine and Rogers [23] reported that process-induced residual stresses alter the martensite and austenite start temperatures of SMA wires embedded in an elastomeric composite. Hebda *et al* [19] also discussed the issue of local residual stresses with regard to manufacturing high-quality SMA composites.

More comprehensive investigations of the interaction between embedded SMA wires and a polymer matrix are provided by Kline *et al* [24] and Jonnalagadda *et al* [25]. The maximum shear stress induced in a polymer matrix due to actuation of a SMA wire was measured photoelastically and correlated with the interfacial bond strength of the SMA–polymer interface. As the level of interfacial adhesion increased, the stresses induced in the matrix also increased. Sottos *et al* [26] used this same photoelastic technique to observe the transformation behavior of embedded SMA wires in a polymeric matrix. Jonnalagadda *et al* [27, 28] extended this work to measure the evolution of stress during the transformation of embedded SMA ribbons. The ribbon geometry was ideal for comparison of experimental data with theoretical predictions.

Several interesting features were observed during the photoelastic experiments. The transformation of the embedded SMA appeared to initiate near the ends and proceed inward along the length of the wire or ribbon. Also, the data indicated only a small percentage of the total length of the embedded SMA ribbon or wire is transformed. Because the stresses induced in the matrix were relatively small (5–15 MPa), the number of fringes generated in the polymer was also small. The low fringe density made it difficult to accurately quantify the initiation and any apparent propagation of the transformation front. In the current work, a new set of experiments is carried out using moiré interferometry to obtain *in situ* whole-field displacement data to complement the stress measurements reported by Jonnalagadda *et al* [27, 28]. The displacement data provide the location of the transformation front during actuation of an embedded ribbon and clearly show how much of the ribbon transforms. The displacement measurements also provide an independent set of data for the evaluation of theoretical models.

Application of existing macroscopic constitutive models to predict embedded SMA response is not straightforward. The models in groups (i), (ii) and (iii) as categorized by Bekker and Brinson [6] are one or two dimensional and may not effectively account for the 3D constraint imposed by the host material. In Jonnalagadda *et al* [28], a constitutive model from group (iv), based on the formalism of Boyd and Lagoudas [29], was adopted to predict the behavior of embedded ribbons. The displacement-based finite-element program ABAQUS was used to solve the history-dependent fully-coupled thermomechanical boundary value problem for an embedded SMA ribbon sample. The thermo-mechanical constitutive model for the SMA ribbon was implemented

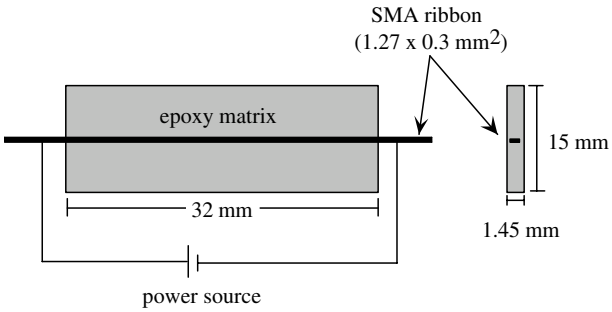

Figure 2. Schematic diagram of the embedded SMA sample.

Table 1. Material properties of SMA ribbon in the austenitic and martensitic phases.

Material property	Austenite	Martensite
E (GPa) [37]	49.0	10.9
v [37]	0.3	0.3
α ($\times 10^{-6}\,^{\circ}C^{-1}$)	12.5	12.5
K (W m$^{-1}\,^{\circ}C^{-1}$) [5]	18.0	8.5
ρ (kg m^{-3}) [5]	6450	6450
C_A (MPa $^{\circ}C^{-1}$) [5]	—	13.5
C_M (MPa $^{\circ}C^{-1}$) [5]	13.5	—
A_f ($^{\circ}$C)	—	57.0
A_s ($^{\circ}$C)	—	35.0
M_s ($^{\circ}$C)	21.0	—
M_f ($^{\circ}$C)	−12.0	—

and integrated with ABAQUS in the form of the subroutine UMAT. A similar procedure is conducted in the current study to calculate displacements and strains to compare with the moiré measurements. Since the thermomechanical coupling due to latent heat effects and various numerical issues have been discussed at great length in previous publications [28, 30–33], only a summary of the constitutive model is presented in this paper where the focus is the comparison of the model predictions with experiment.

2. Experimental procedure

2.1. Sample preparation

Test samples were fabricated by embedding a single SMA ribbon (55% Ni, 45%Ti) 1.27 mm wide and 0.3 mm thick in a room-temperature-cure epoxy matrix. A schematic diagram of the sample is shown in figure 2. The ribbons were annealed at 600 °C for 10 min and then sand blasted in order to maximize the adhesion with the matrix. Annealing mitigates the stresses induced during processing. As a result, very little shape memory effect is observed in annealed ribbons without prestraining. The transformation temperatures of the ribbons were measured using differential scanning calorimetry (DSC) and are listed in table 1 along with other relevant material properties. One set of ribbons was subjected to a uniform strain of 1% and then embedded into the epoxy matrix. A second set of ribbons with no prestrain was embedded into control samples. The control samples were used to evaluate purely thermal displacements due to heating.

Because the presence of residual stress alters the transformation temperatures of the embedded ribbon (see figure 1) and complicates the sample response upon heating, high-temperature-cure matrices were not considered. A room-temperature-cure epoxy resin, EPON 828 (diglycidyl ether of bisphenol A, Shell) cured with Ancamine T (diethylenetriamine (DETA), Air Products) was chosen. The two-part epoxy was thoroughly mixed, degassed for approximately 30 min to remove any air bubbles and then poured into prepared silicon rubber moulds containing a single SMA ribbon. Samples were allowed to cure at room temperature for 10 days. Relevant properties of the cured epoxy matrix are listed in table 2.

Table 2. Material properties of the epoxy matrix.

Material property	Epoxy
E (GPa)	3.5
v	0.33
α ($\times 10^{-6}\,^{\circ}C^{-1}$)	57.0
K (W m$^{-1}\,^{\circ}C^{-1}$)	0.18
ρ (kg m^{-3})	1350
T_g ($^{\circ}$C)	56

As a consequence of the meniscus that formed around the edge of the samples, it was impossible to pour the sample thinner than about 5 mm. Polishing of the samples was necessary to diminish the thickness and to provide a flat surface for use in the interferometer. The final thickness of the prepared samples was approximately 1.45 mm, while the ribbon thickness was 1.27 mm as shown in figure 2. A thin layer of epoxy (∼0.09 mm) was left between the edge of the embedded ribbon and the polished surface to hinder debonding. Even with careful sample preparation, small debonds approximately 2 mm in length formed at the right and left edges of the sample where the ribbon emerged from the polymer block. Optical observation indicated that the initial debonds did not grow during the subsequent experiments.

Diffraction gratings were applied to the samples using the technique described by Post *et al* [34]. First, a submaster of a 1200 lines mm^{-1} cross lined master grating was replicated using GE RTV 615 silicone rubber. The silicone rubber was degassed in a vacuum jar for approximately 10 min until all visible air bubbles had collapsed. A 3 cm diameter pool of the degassed silicone rubber was then poured on a clean and primed glass plate. The master grating was pressed onto the silicone rubber for replication. After allowing the RTV 615 to cure for 24 h, the master and submaster were separated by a specially designed fixture. The fixture permitted the controlled separation of the gratings while minimizing the bending loads on the glass plates. The silicone rubber submaster was then replicated in the same fashion by using a low-viscosity epoxy.

The epoxy grating was coated with aluminum through vacuum evaporation deposition. After evaporating one coat of aluminum onto the epoxy grating, a solution of Kodak Photo-flo 200 (diluted 1:200 in distilled water) was applied. The Photo-flo solution acted as a separating agent between the first layer of aluminum and a second layer, which was evaporated onto the grating after the solution had dried fully. This second grating layer was then transferred to the samples by spreading a thin degassed layer of epoxy onto the samples with the wooden end of a swab and placing the sample onto

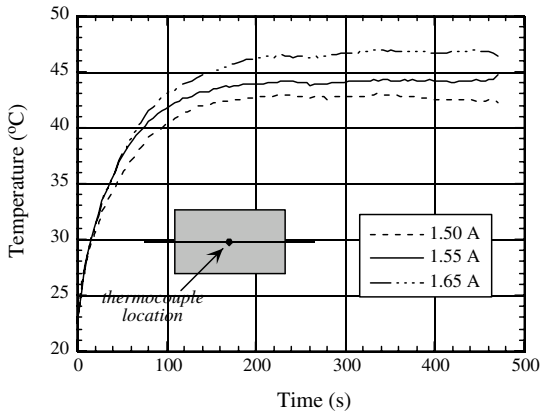

Figure 3. Temperature profiles of the sample surface for different power inputs.

the grating. The orientation of the grating lines required that the perimeter of the specimen be square with respect to the edges of the grating. In this way, moiré fringes corresponded to displacements along the major and minor axes of the specimen.

2.2. Sample heating

The shape memory effect was induced by resistive heating of the embedded ribbons. This method provided a repeatable, easily controlled heating method. As discussed above, the samples were prepared using a room-temperature-cure matrix to minimize the residual stress field in the sample. The disadvantage of the room-temperature-cured epoxy was a low glass transition temperature. For the EPON 828/Ancamine T epoxy, the value of the glass transition ($T_g = 56\,^{\circ}$C) was lower than the austenite finish temperature measured for the ribbons ($A_f = 57\,^{\circ}$C). In order to avoid significant stress relaxation in the matrix, the maximum temperature in the sample had to remain below T_g. In this work, current inputs were chosen so that the temperature of the ribbon did not exceed 47 °C.

The temperature profile of the samples was measured by placing a thermocouple on the polished epoxy surface at the midpoint of the sample. Transient temperature profiles are plotted in figure 3 for three different current inputs. Steady-state temperatures of 42.5, 44 and 47 °C were attained in 240 s for currents of 1.50, 1.55 and 1.65 A, respectively. The uniformity of the temperature profile along the length of the ribbon was verified in previous work by measuring the temperature field of the entire sample with a digital infrared camera [28]. Infrared images demonstrated that the ribbon temperature varied by less than 0.5 °C from the edge of the sample to the center.

2.3. Experimental set-up

Full field displacements of the embedded SMA sample were measured using a compact, four-beam moiré interferometer (PEMI 2001-X, IBM Corporation). Post *et al* [34] provide a detailed description of this instrument. The optics for the four-beam interferometer are enclosed in a single cabinet with only necessary adjustment screws on the outside. The beam

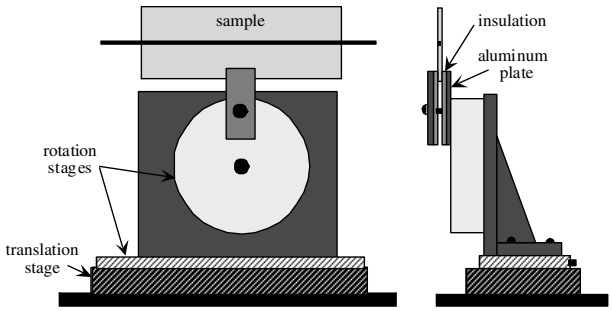

Figure 4. Schematic diagram of the sample fixture.

from a 632 nm He–Ne laser source enters the cabinet through an optical fiber, passes through several lenses to expand and collimate the beam and is incident upon a 1200 line mm^{-1} diffraction grating which divides it into four first-order diffracted beams (plus the zero-order beam, which is not used). Two of the beams are directed by mirrors on opposite sides of the cabinet to create the U field while the other two beams are reflected by mirrors on the top and bottom of the cabinet to form the V field. A baffle is swivelled back and forth to block the beams of either the U field or the V field. The angle of incidence of the beams onto the sample, α, is 49.4° and the resulting frequency of the virtual grating in the interferometer f_v is 2400 lines mm^{-1}, twice the sample grating frequency f. Light diffracted by the specimen grating is collected by a field lens on the front of the cabinet. Test samples are positioned within the 45 mm diameter viewing field of the interferometer using a translation table, rotation stage and the screw adjustments on the interferometer. A pneumatic optical table isolates the entire assembly from ambient vibration.

The sample holder was designed to minimize any effect on the movement of the SMA ribbon. After experimenting with a number of possible designs, the fixture shown schematically in figure 4 was adopted. The sample was clamped in the center along the bottom edge and mounted on a rotation stage. Thermal insulation was placed between the sample and the aluminum plates to avoid heating of the fixture. Additional rotation and translation stages were incorporated for aligning the sample in the interferometer. The exposed ends of the ribbons were connected to a power supply and heated resistively to different temperatures. Displacement of the ribbon was monitored continuously in the axial direction (x_1) using the U-field setting.

The resulting moiré images were recorded by a CCD camera (Panasonic BL200) connected to a VCR (Mitsubishi U82). Images were stored for analysis using a 640 pixel by 480 pixel frame grabber. Displacements and strains in the x_1 direction were calculated from the fringe order using the relationship [34]:

$$U = \frac{1}{f_v} N_x \tag{1}$$

$$\varepsilon_1 = \frac{\partial U}{\partial x_1} = \frac{1}{f_v}\frac{\partial N_x}{\partial x_1} \approx \frac{1}{f_v}\frac{\Delta N_x}{\Delta x_1} \tag{2}$$

where f_v is the virtual grating frequency and N_x is the fringe order in the U field.

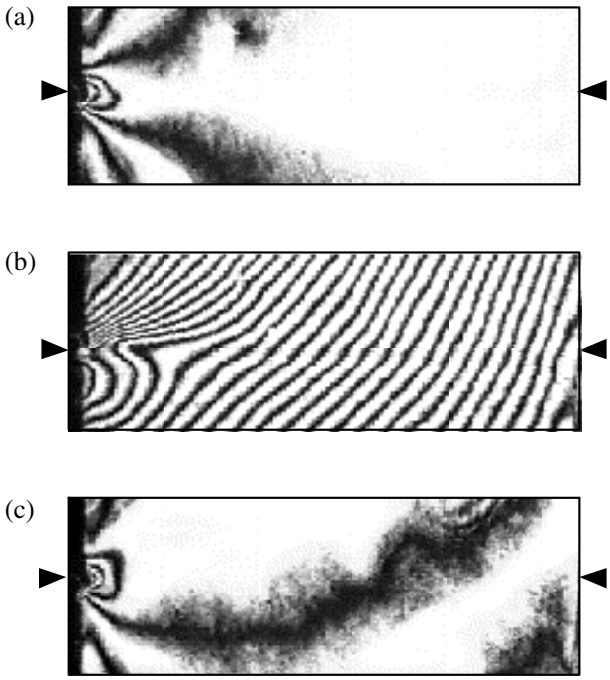

Figure 5. Moiré images of an annealed ribbon sample: (a) prior to heating, (b) at a steady-state temperature of 42.5 °C and (c) after cool down.

3. Displacement measurements

3.1. Control samples

In order to separate purely thermal effects, control samples (annealed SMA ribbons with no prestrain) were tested first using a current input of 1.50 A. The power was switched on and the sample heated to a steady-state temperature of 42.5 °C. The power was then switched off and the sample was allowed to cool to room temperature. Moiré fringe patterns, shown in figure 5, were acquired prior to heating, at steady-state temperature ($t = 240$ s) and after cool down ($t = 480$ s). Due to symmetry, only the left-half of the sample is shown in all of the images. Arrowheads at the side of each figure mark the location of the ribbon in the sample.

Only a few fringes were present in the null field prior to sample heating, as shown in figure 5(a). At the steady-state temperature a large number of uniformly spaced fringes developed across the sample (figure 5(b)) with a slight concentration occurring near the edge of the ribbon. The lack of fringe symmetry about the ribbon axis was caused by the sample fixture. Although attempts were made to rigidly mount and perfectly insulate the sample, the fixture always absorbed some heat by conduction and caused a temperature difference between the top and bottom of the sample. The fixture also permitted a small amount of in-plane rotation and out-of-plane bending of the sample. After cool down, the fringes dissipated and the final pattern was similar to the null field (figure 5(c)). Hence, the displacement fringes at 42.5 °C (figure 5(b)) were mostly thermal with little or no contribution from SMA transformation. The images in figure 5(b) were analyzed and the displacements at steady state were calculated using equation (1).

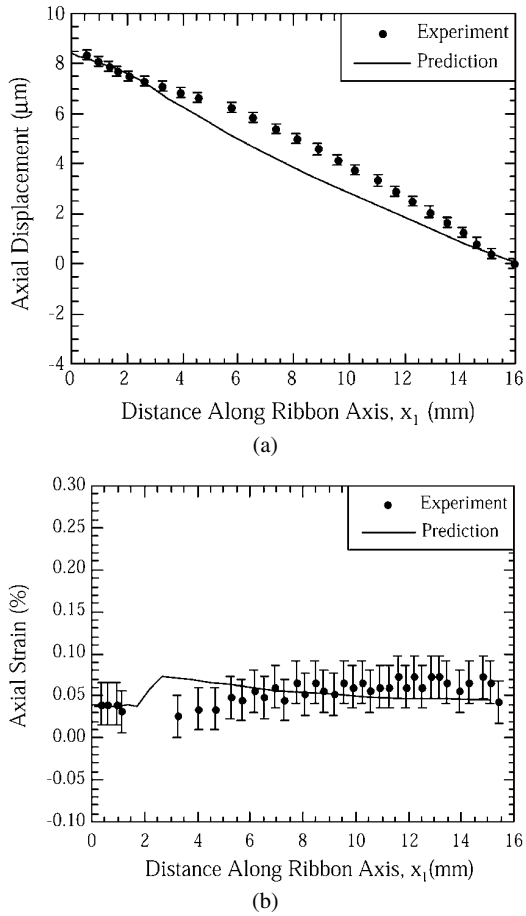

Figure 6. Comparison of experimental and numerical predictions for an annealed SMA ribbon at a steady-state temperature of 42.5 °C: (a) displacement profile and (b) axial strain.

The ribbon displacements at 42.5 °C are plotted in figure 6(a) from the left edge of the sample to the center. For all of the plots, the left edge of the sample is treated as the origin. The displacement is zero in the center of the sample and increases almost linearly until reaching the debond. In the debonded region (2 mm from the edge of the sample), the slope of the displacement curve decreases significantly. Using the method described by Stout *et al* [35], the error in the displacement measurements was estimated to be $\Delta u_1 = \pm 0.2$ μm. The steady-state axial strain, ε_1, in the sample was calculated from equation (2) and plotted in figure 6(b). The measured strain has a nearly constant value of 0.04% in the debonded region and approaches a nearly constant value of 0.06% strain near the center of the sample. The strains are relatively small because they are due to thermal mismatch only. At such small strain values, significant scatter occurs due to the differentiation of the experimental data. Again using the method described by Stout *et al* [35], the error in the strain measurements was estimated to be $\Delta\varepsilon_1 = \pm 0.000\,25$. Similar fringe patterns were repeated for three different samples.

3.2. Prestrained ribbons

The 1% prestrained ribbon samples were also tested by applying a current of 1.50 A. The moiré fringes acquired

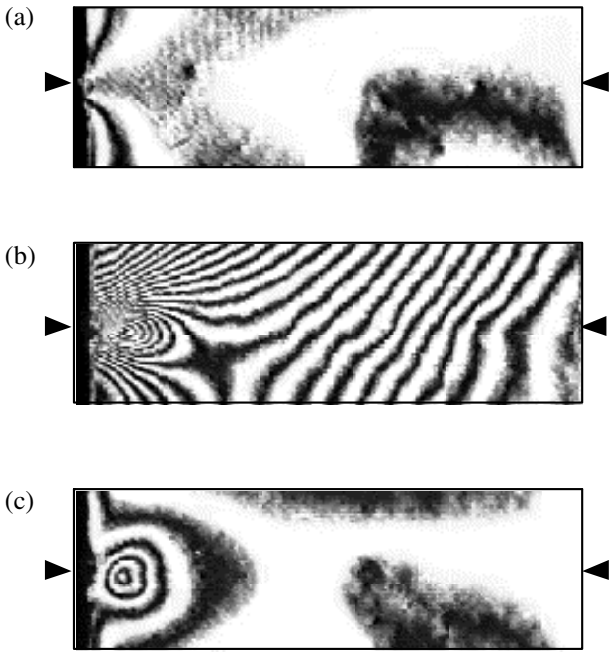

Figure 7. Moiré images of a 1% prestrained ribbon sample: (a) prior to heating ($t = 0$ s), (b) at a steady-state temperature of 42.5 °C ($t = 240$ s) and (c) after cool down ($t = 480$ s).

in the null field, at steady-state temperature ($t = 240$ s), and after complete cool down of the sample ($t = 480$ s), are shown in figures 7(a)–(c), respectively. The fringe patterns for the sample with a prestrained ribbon (figure 7) differ significantly from those of the control sample in figure 5. A distinct saddle point is observed in the fringe patterns at a distance of 4.1 mm from the edge of the sample, indicating a local maximum in the displacement field. Due to the lack of thermal symmetry and rotation caused by the fixture, the saddle point is located slightly below the ribbon axis. The steady-state fringes in figure 7(b) were analyzed and the corresponding displacement and strain profiles plotted in figure 8. The steady-state displacement contour in figure 8(a) is zero at the center of the sample and has a maximum at 4.1 mm from the edge of the sample. The displacements rapidly decrease in the debonded region near the edge of the sample. The axial strain in figure 8(b) has a nearly constant value of 0.25% in the debonded region and rapidly approaches zero with increasing distance along the ribbon.

After cool down, a significant number of residual fringes remain in the prestrained samples (figure 7(c)). This fringe pattern is quite different from the null field (figure 7(a)) indicating a one-way transformation of the prestrained SMA ribbon. The residual fringe patterns in figure 7(c) indicate that most of the transformation is restricted to the portion of the ribbon between the edge of the sample and the outermost fringe. Image analysis showed that the distance of the outermost fringe in figure 7(c) is also 4.1 mm. Hence, the outermost fringe in figure 7(c) and the saddle point in figure 7(b) indicate the location of the transformed region of the SMA. Residual displacement values and the effect of the steady-state temperature are discussed in the next section. Again, fringe patterns were repeatable for three different samples.

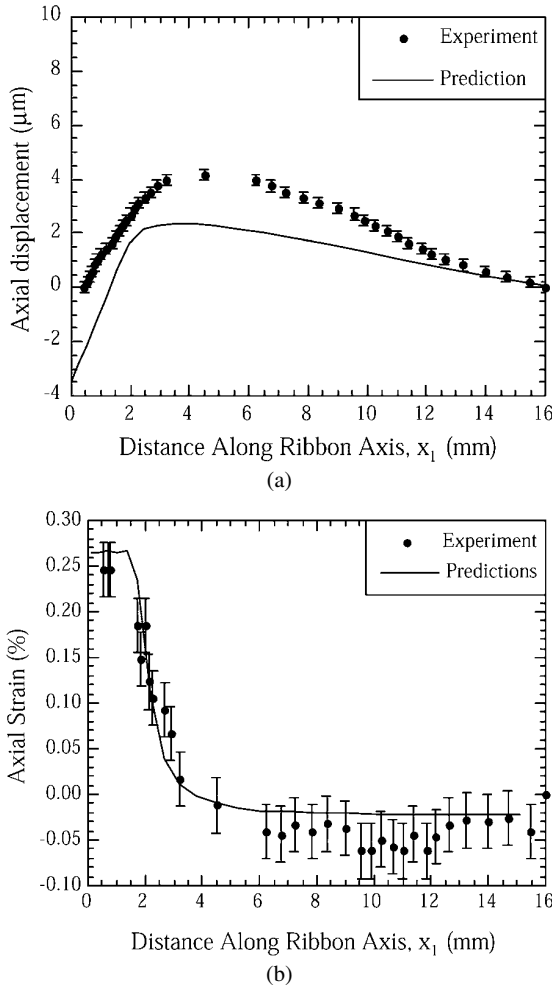

Figure 8. Comparison of experimental and numerical predictions for a 1% prestrained SMA ribbon at a steady-state temperature of 42.5 °C: (a) displacement profile and (b) axial strain.

3.3. Effect of steady-state temperature

Because the SMA ribbons are not heated above the austenite finish temperature (A_f), the amount of phase transformation is dependent on how high the temperature rises above A_s. Additional tests were carried out on 1% prestrained samples at steady-state ribbon temperatures of 44 and 47 °C. At higher temperatures, relaxation of the matrix resulted in distorted fringes near the ribbon. The residual moiré fringe patterns after cool down from all three steady-state temperatures are compared in figure 9. As the steady-state temperature increased, the density of fringes increased, but the location of the outermost fringe only changed slightly. The corresponding displacement and strain profiles calculated from these fringes are plotted in figure 10. Increasing the steady-state ribbon temperature resulted in larger displacements and strains (more negative) near the edge of the ribbon. The maximum residual displacement increased from -1.67 μm for a steady-state temperature of 42.5 °C to -2.5 and -4.2 μm for the ribbons heated to 44 and 47 °C, respectively. The increase in both strain and displacement is caused by a greater fraction of martensite transforming to austenite at higher steady-state temperatures. The size of the transformed region along the length of

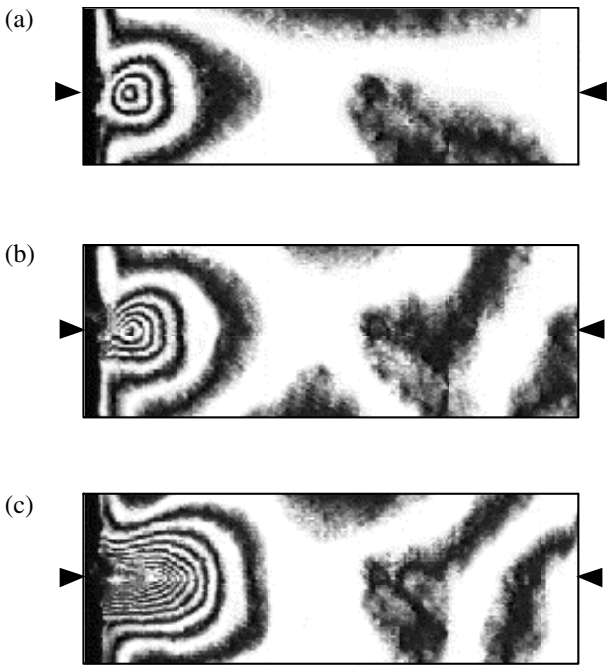

Figure 9. Moiré images of 1% prestrained ribbon sample after cool down from different steady-state temperatures: (a) 42.5 °C ($I = 1.50$ A), (b) 44 °C ($I = 1.55$ A) and (c) 47 °C ($I = 1.65$ A).

the ribbon only increased slightly with temperature. The outermost fringe was located at a distance of 4.8 mm from the edge for the sample heated to 47 °C as compared with 4.1 mm for 42.5 °C.

4. Numerical model

Displacement and strain profiles of the embedded SMA wire were predicted using the finite-element method to solve the history-dependent thermomechanical boundary value problem. The commercial nonlinear finite-element code ABAQUS was used for the analysis, supplemented by a user supplied UMAT containing the numerical implementation of the 3D incremental formulation of the SMA constitutive model developed by Boyd and Lagoudas [29] and Lagoudas *et al* [30]. A fully-coupled temperature–displacement formulation was adopted to analyse the problem. A detailed description of the initial boundary value problem, field equations and constitutive equations is provided in Jonnalagadda *et al* [28]. Key aspects of the numerical analysis are summarized below.

The 3D model of the experimental sample geometry and corresponding boundary conditions are shown schematically in figure 11. The geometry in figure 11 is the upper left quadrant (ABCDEFGH) of the sample shown in figure 2, where t is half of the original depth. Using the symmetry with respect to x_1, x_2 and x_3 axes, the planes defined by FBCG, AEFB and ABCD are constrained to move in the x_1, x_2 and x_3 directions, respectively. Similarly there is no heat flux through the plane FBCG, AEFB and ABCD, due to symmetry. The other mechanical boundary conditions are traction-free surfaces, while free-convection conditions exist where the plate is exposed to air on the upper plane EFGH and

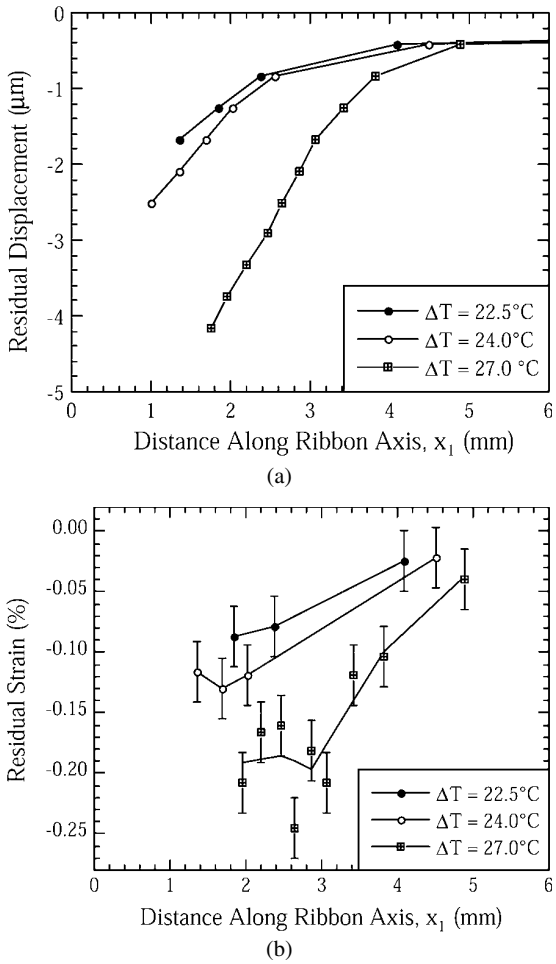

Figure 10. Experimental profiles for a 1% prestrained SMA ribbon after cool down from different steady-state temperatures: (a) displacements and (b) axial strain.

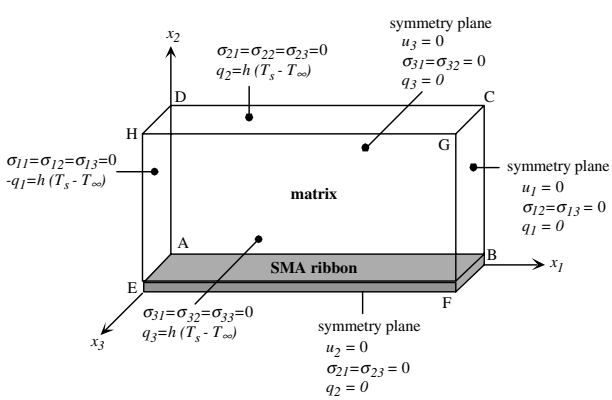

Figure 11. Schematic diagram of finite-element model and boundary conditions.

the sides DHGC and EADH. Both the ambient temperature and the initial temperature of the SMA and epoxy are assumed to be room temperature, i.e. $T_\infty = T_0 = 25.0$ °C. Note that the thermomechanical problem is not driven by the initial boundary conditions, but by the distributed heat source in the SMA ribbon due to resistive (Joule) heating.

The present problem is a strongly coupled thermo-mechanical problem, where the SMA strain hardening

behavior is directly influenced by temperature. The initial boundary value problem thus requires the simultaneous satisfaction of two field equations in both the SMA and epoxy: the equation of equilibrium (balance of linear momentum) assuming body forces and inertial effects are negligible,

$$\sigma_{ij,j} = 0 \tag{3}$$

and the heat equation (balance of energy)

$$\rho c\dot{T} = \rho\dot{Q} + \rho\dot{\Omega}. \tag{4}$$

In equation (3), σ_{ij} is the Cauchy stress tensor, which is assumed to be a function of the infinitesimal total strain tensor, ε_{ij}, the temperature, T, the internal state variable corresponding to the martensitic volume fraction, ξ, and the transformation strain, ε^t_{ij}, for the SMA. For the epoxy, which is assumed to be isotropic elastic (see material properties in table 2), the stress tensor, σ_i, is only a function of the total strain tensor, ε_{ij}, and the temperature, T. In (4), ρ and c are, respectively, the mass density and specific heat of either the SMA or epoxy and $\rho\dot{\Omega}$ is the two-way coupling term between the thermal and mechanical problem. For elastic materials, $\rho\dot{\Omega}$ is negligible and the two-way thermomechanical coupling reduces to one-way coupling, where only stress is dependent on temperature but not *vice versa*. The derivation of $\rho\dot{\Omega}$ for SMA is given in Lagoudas *et al* [30] and Jonnalagadda *et al* [28].

As stated previously, the 3D incremental formulation of the SMA constitutive model developed by Boyd and Lagoudas [29], and Lagoudas *et al* [30] is used to predict the thermomechanical response of the SMA. The constitutive equations describe the infinitesimal total strain, ε_{ij}, in terms of stress σ_{ij}, transformation strain, ε^t_{ij}, temperature, T, and reference temperature, T_0,

$$\varepsilon_{ij} = S_{ijkl}\sigma_{kl} + \alpha_{ij}(T - T_0) + \varepsilon^t_{ij}. \tag{5}$$

The total stress–strain relations in (5) can be inverted and written in an incremental form as

$$\dot{\sigma}_{ij} = C_{ijkl}[\dot{\varepsilon}_{kl} - \alpha_{ij}\dot{T} - Q_{kl}\dot{\xi}] \tag{6}$$

where

$$Q_{ij} = \Delta S_{ijkl}\sigma_{kl} + \Delta\alpha_{ij}(T - T_0) + \Lambda_{ij} \tag{7}$$

and S_{ijkl} is the effective elastic compliance tensor, $C_{ijkl} = (S_{ijkl})^{-1}$ is the effective elastic stiffness tensor, α_{ij} is the effective thermal expansion coefficient tensor and Λ_{ij} is the transformation tensor ($\varepsilon^t_{ij} = \Lambda_{ij}\xi$). The terms that are defined with the prefix Δ in (7) indicate the difference of a quantity between the martensitic and austenitic phases. The evolution equations for ξ and ε^t are not given here for reasons of brevity and can be obtained from any one of [29–32]. The heat transfer equation obtained by using the first law of thermodynamics, the Legendre transformation between the internal energy, u, and the Gibbs free energy, G, and the definition of G for polycrystalline SMA [30] can be explicitly written in terms of $\dot{\xi}$ and $\dot{\sigma}_{ij}$:

$$\rho c\dot{T} - \rho\dot{Q} = (\pi - T\Delta\alpha_{ij}\sigma_{ij} - \rho\Delta s_0 T)\dot{\xi} - T\alpha_{ij}\dot{\sigma}_{ij} \tag{8}$$

Here, s_0 is the specific entropy and π is the thermodynamic force conjugate to ξ which defines the transformation surface. The term on the right-hand side of equation (8) is $\rho\dot{\Omega}$ and provides the two way coupling between the mechanical and thermal parts. Equations (6) and (8) together define the fully-coupled stress–temperature system of equations. To calculate the increment of stress for given strain and temperature increments according to the SMA constitutive model, a return mapping integration algorithm proposed by Ortiz and Simo [36] was used. For details of the implementation, the work by Lagoudas *et al* [30] and Qidwai and Lagoudas [32] can be consulted.

Eight-node brick elements were utilized to discretize the problem domain. A convergence study was performed for 132, 216 and 400 eight-node brick finite elements, respectively. All the results presented here are for the finite-element mesh of 400 elements. Note that only one layer of elements was introduced in the x_3 direction, because of the small thickness of the specimen. The simulations were run for a period of 15 min and the steady state was attained at approximately 4 min. All relevant material properties for the simulation are given in tables 1 and 2.

The 2 mm debonded region between the SMA ribbon and the epoxy matrix at the edge of the sample was modelled by defining contact surfaces with Coulomb friction coefficient of $\mu = 0.5$, obtained from SMA fiber–epoxy matrix pull-out experiments [25]. A large value for the gap conductivity between the contact surfaces is chosen such that it ensures a zero temperature jump across the debonded area. The previous numerical simulations by Jonnalagadda *et al* [28] underscored the critical effect of the debonded area on the correct prediction of stress contours and phase transformation. The absence of a debonded area caused the stress concentration to shift towards the free edge, resulting in a lower thermodynamic driving force and thus less transformation near the edge than the fully bonded case.

5. Comparison of numerical predictions and experiment

Numerical simulations were first carried out for the control samples with a current input of 1.5 A, corresponding to a steady-state temperature of 42.5 °C in the ribbon. Displacements and strains were calculated assuming that the epoxy matrix and the annealed SMA ribbons in the control samples were linear elastic and did not exhibit any SMA effect. The displacement profile obtained from the finite-element solution is plotted with the steady-state displacement curve measured using moiré interferometry in figure 6(a). The numerical predictions and experimental measurements are in good overall agreement, particularly in the debonded region of the ribbon ($x_1 < 2$ mm). In the bonded region, the experimental curve has a slight positive curvature while the predicted displacement values have a slight negative curvature. As a result of the differences in curvature, the predicted values are a maximum of 20% lower than the experimental values. Predictions of axial strain in the control sample are plotted with experimental values in figure 6(b). The experimental and numerical strain values are in good agreement in the debonded region and throughout the central

portion of the sample. However, in the region next to the debonded region (2 mm $< x_1 <$ 4 mm), the strain predictions differ more significantly due to the difference in curvatures of the displacement profiles in figure 6(a).

The observed differences between experiment and theory may be attributed to several factors. First, the influence of the sample fixture was not accounted for in the simulation. The sample was mounted only from the bottom edge (see figure 4) which caused a non-uniformity in the temperature displacement profiles and allowed small amounts of in-plane rigid body rotation and out-of-plane bending of the sample about the fixture. Second, the sample had a thin layer of epoxy remaining between the ribbon surface and the front and back faces of the sample (see figure 2) that was also not accounted for in the finite element-model (figure 11). Finally, some of the material properties in tables 1 and 2 were taken from the literature and may not be exact.

Numerical simulations were also carried out for the 1% prestrained ribbon samples. For this case, displacements and strains were calculated using the incremental formulation of the SMA constitutive model (summarized in section 4) for the ribbon. The epoxy matrix was still assumed to be linear elastic. The predicted displacement profiles are plotted with the experimental measurements in figure 8(a). The numerical and experimental displacement curves have the same overall shape, but the predicted values are significantly lower. As for the control samples, the differences between the experimental and predicted displacement profiles in figure 8(a) are most likely due to the effects of the sample fixture and the thin epoxy layer which were not accounted for in the modeling. The fringe patterns in figure 7 also indicate that some in-plane rigid body rotation occurred as the ribbon actuated. In previous simulations of photoelastic fringe patterns [28] where rotations were not an issue, this type of discrepancy between theory and experiment was not observed. While rotation affects the displacement measurements, it does not influence the experimental strains. The corresponding predictions of axial strain in figure 8(b) are in excellent agreement with experimental values. Of particular significance, both the numerical simulation and experiments clearly indicate that only the portion of the ribbon near the edge of the sample ($x_1 <$ 4 mm) transforms.

The absence of transformation in the center portion of the embedded ribbon can be attributed to the constraint imposed by the surrounding matrix. Due to load transfer between the matrix and the stiffer SMA ribbon, axial stress in the ribbon builds up from zero at the free edge of the sample to a maximum value at the center. As discussed previously, the austenitic transformation temperature increases linearly with applied stress (figure 1). Near the edge of the sample, the stress in the ribbon is lower and the shift in transformation temperatures is therefore smaller. As a result, most of the transformation occurs near the edge of the sample for a given steady-state temperature. The non-uniform transformation of the ribbons has important implications for designing and predicting the behavior of embedded SMA actuators. Partial SMA transformation will result in much different composite response than full transformation.

6. Conclusions

The *in situ* displacements and strains of SMA ribbons embedded in an epoxy matrix were measured using moiré interferometry. Measurements were made for 1% prestrained SMA samples actuated by resistive heating. Analysis of the resulting fringe patterns at steady-state temperature and after cool down indicated that most of the phase transformation in the SMA ribbon was restricted to a region close to the edge of the sample. The outermost residual fringe indicated the location of the phase transformation front upon cool down. The location of a saddle point at the steady-state temperature matched the location of the outermost fringe in the sample after cool down, indicating the location of the phase transformation front during heating. Increasing the steady-state temperature of the sample induced further transformation in the partially transformed region between the edge of the sample and the actuation front, but resulted in only a small movement of the transformation front. Numerical simulations of the embedded ribbon were carried out using a fully-coupled thermomechanical SMA constitutive model. Overall, the numerical predictions were in good agreement with both the measured displacements and strains in the ribbon, supporting the result that only the portion of the embedded ribbon near the end of the sample transforms.

References

[1] Ölander A 1932 The crystal structure of AuCdZ *Kristallograph.* **83** 145–8

[2] Buehler W J, Gilfritch J V and Riley R C 1963 Effect of low-temperature phase changes on the mechanical properties of alloys near composition of TiNi *J. Appl. Phys.* **34** 1475–7

[3] Wayman C M 1989 An introduction to martensite and shape memory *Engineering Aspects of Shape Memory Alloys* ed T W Deurig *et al* (Boston, MA: Butterworth–Heinemann) pp 3–20

[4] Schuerch H U 1968 Certain physical properties and applications of Nitinol *NASA Report* Cr-1232, NTIS N 69-11420, pp 1–23

[5] Dye T E 1990, An experimental investigation of the behavior of Nitinol *MSc Thesis* Virginia Tech, Blacksburg, VA, USA

[6] Bekker A and Brinson L C 1997 Temperature induced phase transformation in a shape memory alloy: phase diagram based kinetic approach *J. Mech. Phys. Solids* **45** 949–88

[7] Shaw J A and Kyriakides S 1995 Thermomechnical aspects of NiTi *J. Mech. Phys. Solids* **43** 1243–81

[8] Shaw J A and Kyriakides S 1995 On the nucleation and propagation of phase transformation fronts in a NiTi alloy *Acta Mater.* **45** 683–700

[9] Leo P H, Shield T W and Bruno P 1993 Transient heat transfer effects on pseudoelastic behavior of shape memory alloy wires *Acta Metall.* **41** 2477–85

[10] Dalaey L and Thienel J 1975 *Shape Memory Effects in Alloys* ed J Perkins (New York: Plenum) pp 341–50

[11] Miyazaki S 1990 Thermal and stress cycling effects and fatigue properties of Ni–Ti alloys *Engineering Aspects of Shape Memory Alloys* ed T W Deurig *et al* (Boston, MA: Butterworth–Heinemann) pp 394–413

[12] Miyazaki S, Otsuka K and Suzuki Y 1981 Transformation pseudo-elasticity and deformation behavior in a Ti–50.6 at% Ni alloy *Scr. Metall.* **15** 287–92

[13] Ling H C and Kaplow R 1981 Variation in the shape recovery temperature in NiTi alloys *Mater. Sci. Eng.* **48** 241–7

[14] Jackson C M, Wagner H J and Wasilewski R J 1963 55-Nitinol—the alloy with a memory: its physical metallurgy, properties, and applications *NASA Report* SP-5110

[15] Wasilewski R J 1971 The effects of applied stress on the martensitic transformation in NiTi *Metall. Trans.* **2** 2973–81

[16] Liang C, Jia J and Rogers C 1989 Behavior of shape memory alloy reinforced composite plates part II: results *Proc. 30th Structures, Structural Dynamics and Materials Conf.* AIAA-89-1331-CP pp 1504–13

[17] Baz A and Ro J 1992 Thermo-dynamic characteristics of Nitinol reinforced composite beams *Composites Eng.* **2** 527–42

[18] Chaudry Z and Rogers C 1991, Response of composite beams to an internal actuator force *Proc. 32nd Smart Structures and Materials Conf.* AIAA-91-1166-CP pp 186–93

[19] Hebda D A, Whitlock M E, Ditman J B and White S R 1995 Manufacturing of adaptive graphite/epoxy structures with embedded Nitinol wires *J. Intell. Mater. Smart Syst.* **6** 220–8

[20] Paine J S N, Jones W M and Rogers C A 1992 Nitinol actuator to host composite interfacial adhesion in adaptive hybrid composites *Proc. 33rd Structures, Structural Dynamics and Materials Conf.* AIAA-92-2405-CP pp 556–65

[21] Paine J S N and Rogers C A 1993 Characterization of interfacial shear strength between SMA actuators and host composite material in adaptive composite material systems *Adaptive Structures and Material Systems* ASME, vol AD-35, pp 63–70

[22] Bidaux J E, Bataillard L, Manson J A and Gotthardt R 1993 Phase transformation behavior of thin shape memory alloy wires embedded in a polymer matrix composite *Proc. 3rd Eur. Conf. on Advanced Materials and Processes* pp 1–5

[23] Paine J S N and Rogers C A 1991 The effect of thermoplastic composite processing on the performance of embedded Nitinol actuators *J. Thermoplast. Composite Mater.* **2** 102–22

[24] Kline G, Jonnalagadda K D and Sottos N R 1995 Correlating interfacial properties with stress transfer in SMA composites *Adapt. Mater. Syst.* **206** 121–8

[25] Jonnalagadda K D, Kline G E and Sottos N R 1997 Local displacements and load transfer in shape memory alloy composites *Experiment. Mech.* **37** 82–90

[26] Sottos N R, Kline G E, Qidwai M A and Lagoudas D C 1996 Analysis of phase transformation fronts in embedded shape memory alloy composites *Proc. SPIE Mathematics and Control in Smart Structures* **2715** 427–38

[27] Jonnalagadda K D, Sottos N R, Qidwai M A and Lagoudas D C 1997 Transformation of embedded shape memory alloys ribbons *Proc. SPIE Mathematics and Control in Smart Structures* **3039** 242–53

[28] Jonnalagadda K D, Sottos N R, Qidwai M A and Lagoudas D C 1998 Transformation of embedded shape memory alloys *J. Intell. Mater. Syst. Struct.* **9** 379–90

[29] Boyd J G and Lagoudas D C 1996 A thermodynamical constitutive model for shape memory materials. 1. The monolithic shape memory alloy *Int. J. Plasticity* **12** 806–42

[30] Lagoudas D C, Bo Z and Qidwai M A 1996 A unified thermodynamic constitutive model for SMA and finite element analysis of active metal matrix composites *Mech. Composite Mater. Struct.* **3** 155–79

[31] Lagoudas D C, Moorthy D, Qidwai M A and Reddy J N 1997 Modeling of the thermomechanical response of active composite laminates with SMA layers *J. Intell. Mater. Syst. Struct.* **8** 476–88

[32] Qidwai M A and Lagoudas D C 2000 Numerical implementation of a shape memory alloy thermomechanical constitutive model using return mapping algorithms *Int. J. Numerical Methods Eng.* **47** 1123–68

[33] Qidwai M A and Lagoudas D C 2000 On thermomechanics and transformation surfaces of polycrystalline shape memory alloy materials *Int. J. Plasticity* at press

[34] Post D, Han B and Ifju P 1994 *High Sensitivity Moiré* (New York: Springer)

[35] Stout E A, Sottos N R and Skipor A F 2000 Mechanical characterization of plastic ball grid array package flexure using moiré interferometry *IEEE Trans. Components, Packaging Manufact. Technol.* B, at press

[36] Ortiz M and Simo J C 1986 An analysis of a new class of integration algorithms for elastoplastic constitutive relations *Int. J. Numerical Methods Eng.* **23** 353–66

[37] Ditman J, White S R and Bergman L 1991 Tensile testing of Nitinol wire *Technical Report* UILU ENG 91-0508, University of Illinois, Urbana, IL, USA